Spectral and carrier transfer characteristics of 1.55-μm InAs/InP coupled-quantum-dot lasers

Zhiyuan Lin, Zhuoran Wang,[*] and Guohui Yuan

School of Optoelectronic Information, University of Electronic Science and Technology of China, North Jianshe Road, Chengdu 610054,
Sichuan Province, People's Republic of China

To explore the spectral and carrier transfer characteristics of 1.55-μm InAs/InP coupled-quantum-dot lasers (CQDLs), we develop a probabilistically coupled multipopulation rate equation model (PCMPREM) involving intradot and interdot relaxation, inhomogeneous broadening, and homogeneous broadening. After solving the PCMPREM with the fourth-order Runge-Kutta method, a simultaneous quadruple lasing spectrum is observed and explained by both the carrier competition theory and coupled theory. An analysis of the results shows that the coupling strength between different subbands changes with different current injections, giving a systematic understanding of the operation of CQDLs systems. With a lower threshold, the CQDL has a much broader output range of more than 105.3 nm around 1.55 μm, which is 7.8 times greater than the uncoupled QDL, indicating that CQDLs can be excellent light sources for not only long-haul ultrahigh capacity optical communications, but also on-chip photonics integrated circuits with low power consumption.

I. INTRODUCTION

During the past decade, quantum-dot lasers (QDLs) have drawn a great deal of attention due to their interesting characteristics such as ultralow threshold current [1], temperature stability [1], ultrawide modulation wavelength range, and chirpless behavior [2]. There are two types of QDLs, i.e., coupled QDLs (CQDLs) and uncoupled QDLs (UQDLs). In CQDLs systems, quantum dots (QDs) located in the same or different layer have the intralayer or interlayer coupling mechanisms between them such as electronic wave function overlap in dense ($\sim 10^{11}$–10^{12} cm^{-2}) QDs arrays [3,4], QDs chains [5,6], vertical coupling between adjacent QDs stacks due to some special structural alignment [7–9], and phonon-assisted coupled tunneling [10]. Compared to UQDLs, CQDLs are demonstrated, both experimentally [4,6,8,9] and numerically [11,12], to have more advantages such as low threshold, narrow lasing linewidth, ultrafast carrier dynamics, and high internal efficiency as well as high output power, promising their applications in fields such as power-efficient light generation, infrared wideband detecting, ultrafast modulation, and quantum computing [13].

In devices with coupled QDs structures (DCQDSs), the above coupling effects have strong influences on the carrier transfer processes, i.e., capture, recombination, relaxation, recovery, and tunneling, which are highly relevant with the unique features of DCQDSs. With specific investigations of the carrier dynamics of DCQDSs, how the mechanisms of the interdot or intradot carrier transfer characteristics affect the operations and the output characteristics of corresponding devices will be well understood to subsequently guide the device fabrication and optimization. Therefore, to obtain high-performance DCQDSs, it is very important to clarify their spectral characteristics, especially the carrier transfer characteristics among different subbands.

However, up to now, only one general description of the spectral characteristics induced by coupling effects, carriers

in the ground state of small-size QDs (SQDs) coupled to the ground state of large-size QDs (LQDs) [4,9,11,14], has been reported and a complete understanding of coupled carrier transfer characteristics is lacking. Meanwhile, the 1.55-μm wavelength is quite meaningful for the optical communication society and corresponding QDLs can be approached by growing InAs QDs on an InP substrate [15]. However, investigations of coupled carrier transfer processes have mainly focused on 1.3-μm InAs/GaAs QDLs [3,4,6,8,14,16,17] and the ones in 1.55-μm InAs/InP QDLs are still less frequently explored.

Driven by above factors, in this paper we propose a probabilistically coupled multipopulation rate equation model (PCMPREM) by taking into account homogeneous broadening (HB), inhomogeneous broadening (IHB), and the intralayer and interlayer coupling to investigate more systematically the spectral behaviors and carrier transfer characteristics of the InAs/InP-based CQDLs. This article is organized as follows. The PCMPREM is described and given in Sec. II. Detailed results and a discussion of the carrier transfer characteristics of CQDL systems and a comparison between the spectra of CQDLs and UQDLs are presented in Sec. III. A summary is given in Sec. IV.

II. DESCRIPTION OF THE PCMPREM

In this PCMPREM, only three energy levels are considered, including the wetting layer (WL), excited state (ES), and ground state (GS), with degeneracies being $\rho_{\mathrm{WL\,eff}}$, 4, and 2 respectively. With the capture times $\tau_{\mathrm{ES}_n}^{\mathrm{WL}}$ and $\tau_{\mathrm{GS}_k}^{\mathrm{WL}}$, respectively, carriers relax into nth subband of the ES (ES$_n$) directly and into the kth subband of the GS (GS$_k$) through an introduced direct relaxation channel [18], which is not included in the rate equations model for 1.3-μm InAs/GaAs QDLs [18–20], after being directly injected into the common carrier reservoir, the WL. Subsequently, for carriers in ES$_n$, there are several paths to transfer such as relaxing to GS$_k$ under the assistance of phonons, emitting by releasing their energy E_{ES_n}, or thermally escaping into the WL. Carriers in GS$_k$ experience the same processes as the ones in ES$_n$. Meanwhile, carriers in the WL, ES$_n$, and GS$_k$ recombine spontaneously within $\tau_{\mathrm{WL}}^{\mathrm{spon}}$, $\tau_{\mathrm{ES}_n}^{\mathrm{spon}}$,
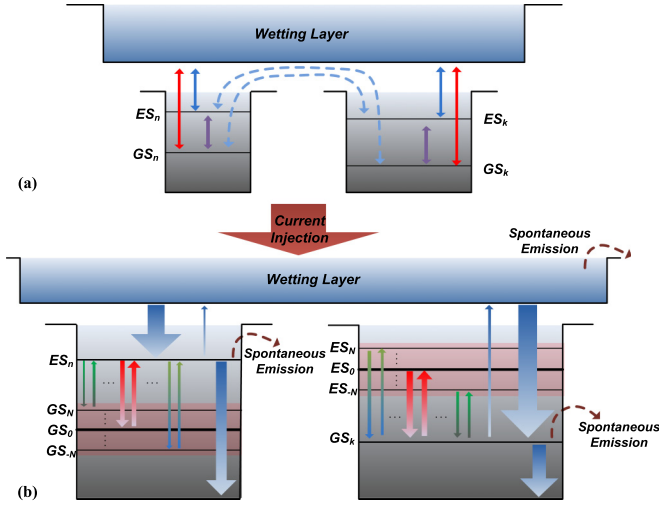
_____
[*]wangzhuoran@uestc.edu.cn

FIG. 1. (Color online) Schematic diagrams of the energy band of the active region with (a) two newly established channels plotted as dashed arrow lines and (b) the reconstructed model for the analysis of the carriers in the sublevels of the ES and GS.

and $\tau_{GS_k}^{spon}$, respectively. It is assumed that all QDs are neutral and electrons and holes are treated as electron-hole pairs, i.e., the holes follow the actions of electrons. The leakage current and the carrier thermal escape effect in the active region and the homogeneous broadening effect induced by the change of carrier density [21] are all ignored.

All processes in the active region described above are illustrated in Fig. 1. In Fig. 1(a), to take into account the correlation of two different subgroups within HB, by assuming that the carriers coupled between adjacent QDs are not captured into the WL but directly into nearby QDs, two new channels are established: the $ES_n - GS_k$ and $ES_k - GS_n$ channels represented by two dashed line. Simultaneously, two intraband channels between ES_n and ES_k, GS_n and GS_k, can also be indirectly built due to the phonon-assisted carrier transfer processes $ES_n - GS_n$ and $ES_k - GS_k$. Considering the correlations of all subgroups, the model is reconstructed, as shown on the left in Fig. 1(b), by including $2N + 1$ paths between ES_n and all subgroups of the GS when analyzing the carrier number on ES_n. Shown on the right in Fig. 1(b) are the same processes in GS_k.

All the processes involved in our PCMPREM are listed as follows:

$$\frac{dN_{WL}}{dt} = \frac{I}{e} + \sum_{n=-N}^{N} \frac{N_{ES_n}}{\tau_{WL}^{ES_n}} + \sum_{k=-N}^{N} \frac{N_{GS_k}}{\tau_{WL}^{GS_k}} - \frac{N_{WL}}{\overline{\tau_{ES}^{WL}}}$$
$$- \frac{N_{WL}}{\overline{\tau_{GS}^{WL}}} - \frac{N_{WL}}{\tau_{WL}^{spon}}, \quad (1)$$

$$\frac{dN_{ES_n}}{dt} = \frac{N_{WL}}{\tau_{ES_n}^{WL}} + \sum_{k=-N}^{N} \frac{N_{GS_k}}{\tau_{ES_n}^{GS_k}} P_{ES_n} - \frac{N_{ES_n}}{\tau_{WL}^{ES_n}}$$
$$- \sum_{k=-N}^{N} \frac{N_{ES_n}}{\tau_{GS_k}^{ES_n}} - \frac{N_{ES_n}}{\tau_{ES}^{spon}} - \Gamma v_g \sum_{m=-M}^{M} g_{mn\,ES} S_m, \quad (2)$$

$$\frac{dN_{GS_k}}{dt} = \frac{N_{WL}}{\tau_{GS_k}^{WL}} + \sum_{n=-N}^{N} \frac{N_{ES_n}}{\tau_{GS_k}^{ES_n}} - \frac{N_{GS_k}}{\tau_{WL}^{GS_k}}$$
$$- \sum_{n=-N}^{N} \frac{N_{GS_k}}{\tau_{ES_n}^{GS_k}} P_{ES_n} - \frac{N_{GS_k}}{\tau_{GS}^{spon}} - \Gamma v_g \sum_{m=-M}^{M} g_{mkGS} S_m, \quad (3)$$

$$\frac{dS_m}{dt} = \Gamma v_g \left(\sum_{n=-N}^{N} g_{mn\,ES} + \sum_{k=-N}^{N} g_{mkGS} \right) S_m - \frac{S_m}{\tau_p}$$
$$+ \beta \left(\sum_{n=-N}^{N} B_{ES}(E_m - E_{ES_n}) \frac{N_{ES_n}}{\tau_{ES}^{spon}} \right.$$
$$\left. + \sum_{k=-N}^{N} B_{GS}(E_m - E_{GS_k}) \frac{N_{GS_k}}{\tau_{GS}^{spon}} \right) \Delta E_m, \quad (4)$$

with N_{WL}, N_{ES_n}, and N_{GS_k} denoting the carrier number in the WL, ES_n, and GS_k, respectively, I the injection current, v_g the group velocity in the active region, Γ the optical confinement factor, and β the spontaneous emission coupling efficiency. The term S_m/τ_p in Eq. (4) is the loss of the photons in the cavity, τ_p is the average lifetime of the photons given as $\tau_p = 1/v_g(\alpha_i + \alpha_m)$, with α_i being the internal loss and α_m the mirror loss given as $\alpha_m = 1/(2L_{ca})\ln(1/R_1 R_2)$, where R_1 and R_2 are the refractive indices of the two mirrors of the cavity, and L_{ca} is the length of laser cavity. In addition, $\overline{\tau_{ES}^{WL}}$ and $\overline{\tau_{GS}^{WL}}$ are the average relaxation lifetime of the ES and GS, respectively, calculated by

$$\overline{\tau_{ES,GS}^{WL}}^{-1} = \sum_{n,k=-N}^{N} \tau_{ES_n,GS_k}^{WL}{}^{-1} G_{ES_n,GS_k}, \quad (5)$$

where G_{ES_n,GS_k} is the Gaussian probabilistic distribution index of the ES and GS, given as [22]

$$G_{ES_n,GS_k} = \frac{1}{\sqrt{2\pi}\xi_0} \exp\left(-\frac{(E_{ES_n,GS_k} - E_{ES_0,GS_0})^2}{2\xi_0^2} \right), \quad (6)$$

with E_{ES_0,GS_0} the energy of the central subgroup of the ES and GS and $\xi_0 = \Gamma_0/2.35$, where Γ_0 is IHB of the QD ensemble caused by the QDs size fluctuation. With the carrier density in the WL, the unoccupied probability, the distribution of the sublevels, and the coupling effects being considered, the related capture time and relaxation time in PCMPREM are given as follows:

$$\tau_{ES_n}^{WL} = \frac{1}{(A_W + C_W N_{WL}/V_{WL})P_{ES_n}G_{ES_n}}, \quad (7)$$

$$\tau_{GS_k}^{ES_n} = \frac{1}{(A_E + C_E N_{WL}/V_{WL})P_{GS_k}G_{ES_n}G_{GS_k}}, \quad (8)$$

$$\tau_{GS_k}^{WL} = \frac{1}{(A_W + C_W N_{WL}/V_{WL})P_{GS_k}G_{GS_k}}. \quad (9)$$

The coefficients A_W, C_W, A_E, and C_E show how the phonon-assisted and Auger effects affect the dynamic processes under different injection rates [23]. The major change is that the factors mentioned above are all considered in all three equations. In particular, in Eq. (8), the term $G_{ES_n}G_{GS_k}$ characterizes the possibility to find a carrier transfer process

between ES_n and GS_k. The assumption is made that the QDs with different sizes have a lateral and vertical uniform position distribution in the active region, so the strengths of relaxation and coupling processes between different subgroups of the ES and GS depend on their state number, which means that it is much easier to achieve the coupling among the QDs with larger quantities. The larger the term $G_{ES_n}G_{GS_k}$ is, the smaller the relax time between ES_n and GS_k will be and a stronger correlation will happen. Therefore, all the processes of possible channels of interdots or intradots can be described by the matrix of the relax time and the escape time. The diagonal elements of the time matrix depict the corresponding intradot processes of the UQDLs in Refs. [24,25]. By using the Gaussian index product term, the coupling effect is quantitatively taken into account, resulting in the changes in Eqs. (2) and (3) and giving a better systematic understanding of the PCMPREM together with the schematic diagrams.

As the Pauli blocking factor, the term P_{ES_n,GS_k} used above is the unoccupied probability in the corresponding subsets of the QDs ensemble, written as

$$P_{ES_n,GS_k} = 1 - \frac{N_{ES_n,GS_k}}{\mu_{ES,GS} N_d w L_{ca} N_l G_{ES_n,GS_k}}, \qquad (10)$$

with $\mu_{ES,GS}$ denoting the degeneracy of the corresponding energy levels, N_d the QD surface density, N_l the number of QD layers, and w and L_{ca} the width and the length of the active region, respectively. The numerator in Eq. (10) is the total carrier state number in the corresponding state.

Without any extra external excitations, it is assumed that the carriers are in the thermal equilibrium state, so the carrier escape times can be given as [20,24,25]

$$\tau_{ES_n}^{GS_k} = \tau_{GS_k}^{ES_n} \frac{\mu_{GS}}{\mu_{ES}} e^{(E_{ES_n}-E_{GS_k})/k_B T}, \qquad (11)$$

$$\tau_{WL}^{ES_n} = \tau_{ES_n}^{WL} \frac{\mu_{ES} N_d N_l}{\rho_{WL\,eff}} e^{(E_{WL}-E_{ES_n})/k_B T}, \qquad (12)$$

$$\tau_{WL}^{GS_k} = \tau_{GS_k}^{WL} \frac{\mu_{GS} N_d N_l}{\rho_{WL\,eff}} e^{(E_{WL}-E_{GS_k})/k_B T}. \qquad (13)$$

We assume that the WL is an ensemble consisting of an effective density of states and the effective degeneracy of the WL can be given as $\rho_{WL\,eff} = \frac{m*}{\pi \hbar^2} k_B T A_{WL} N_l$ [20] with $m*$ the effective electron mass and A_{WL} the area of WL. The terms $g_{mn\,ES}$ and $g_{mk\,GS}$ in the rate equations above are the material gain of ES_n and GS_k, respectively, defined as follows [22,25]:

$$g_{mn\,ES} = \mu_{ES} C_g \frac{|P_{ES}^\sigma|^2}{E_{ES_n}} (1 - 2P_{ES_n}) G_{ES_n} B_{ES}(E_m - E_{ES_n}), \qquad (14)$$

$$g_{mk\,GS} = \mu_{GS} C_g \frac{|P_{GS}^\sigma|^2}{E_{GS_k}} (1 - 2P_{GS_k}) G_{GS_k} B_{GS}(E_m - E_{GS_k}), \qquad (15)$$

where $C_g = \frac{\pi e^2 \hbar}{c n_g \varepsilon_0 m_0^2} \frac{N_d}{H}$, H denotes the average height of the QDs, n_g is the refractive index, m_0 debotes the rest electron mass, and $|P_{ES,GS}^\sigma|^2$ and $B_{ES,GS}(E_m - E_{ES_n,GS_k})$ are the transition matrix momentum [22,26] and the homogenous broadening function [22], respectively,

TABLE I. Simulation parameters.

Symbol	Description	Value
N_d	QD surface density[a]	1×10^{15} m^{-2}
N_l	number of QD layers[a]	3
w	width of the active region	12×10^{-6} m
L_{ca}	length of the active region	0.25×10^{-3} m
R_1, R_2	reflect indices of two cavity mirrors[b]	0.3
α_i	internal loss[c]	6×10^2 m^{-1}
Γ	optical confinement factor[a]	0.036
β	spontaneous emission coupling efficiency[c]	10^{-4}
Γ_0	inhomogeneous broadening[d]	41 meV
Γ_{hom}	homogeneous broadening[a]	20 meV
E_{WL}	emission energy of the WL[a]	1.050 eV
E_{ES_0}	central emission energy of the ES[a]	0.840 eV
E_{GS_0}	central emission energy of the GS[a]	0.792 eV
T	temperature	300 K
$2N+1$	number of QD subgroups	101
$2M+1$	number of spectral groups	1001

[a]Reference [25].
[b]Reference [19].
[c]Reference [22].
[d]Reference [27].

defined as

$$|P_{ES,GS}^\sigma|^2 = 2.70 m_0 E_{ES,GS}, \qquad (16)$$

$$B_{ES,GS}(E_m - E_{ES_n,GS_k}) = \frac{\Gamma_{hom}/2\pi}{(E_m - E_{ES_n,GS_k})^2 + (\Gamma_{hom}/2)^2}, \qquad (17)$$

with E_m the energy of the output mode and Γ_{hom} the HB. The parameters used in the simulation are given in Table I.

III. NUMERICAL RESULTS AND ANALYSIS

A. Carrier transfer characteristics of CQDLs

Plotted in Fig. 2 are the spectral responses of CQDLs at different injection currents obtained by numerically solving the PCMPREM with the fourth-order Runge-Kutta method.
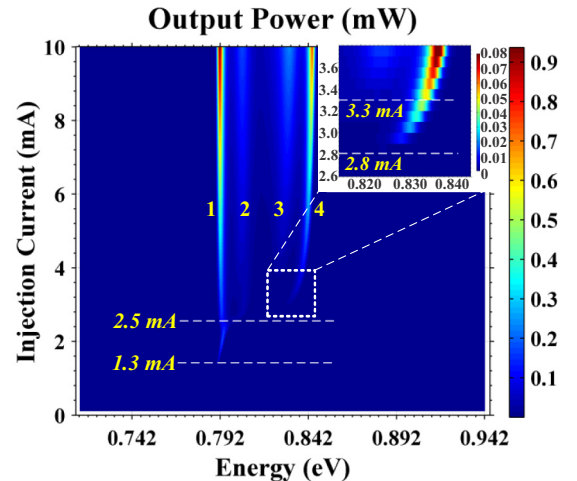

FIG. 2. (Color online) Calculated output spectrum of the PCM-PREM with an original Gaussian index matrix.
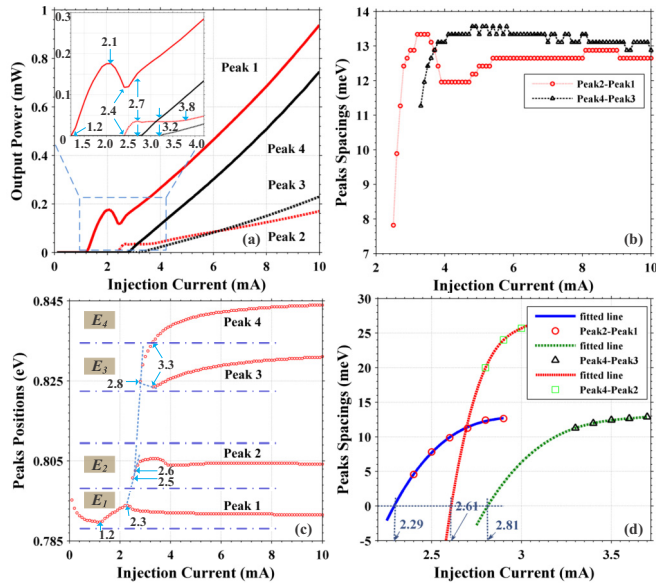
FIG. 3. (Color online) Extracted information of the output spectrum of the PCMPREM with the (a) output power and (c) peak positions of the corresponding four output peaks. The three dashed lines in (c) show potential connections among the four peaks. For convenience, energy levels around the emitting subgroups are divided into four sets, separated by dash-dotted lines: (b) the peak spacings among them with the virtual converge points being marked with dashed line and arrows and (d) the fitted lines of some selected data in (b).

The central GS levels reach their thresholds at 1.3 mA and start emitting. The second emission peak at the higher GS energy turns on at 2.5 mA and shifts first to a shorter wavelength and then to a longer one. An ES peak, namely, peak 4, occurs around 2.8 mA and moves to higher subgroups and remains stable with the increase of injection current. As the excitation increases further to 3.3 mA, peak 3 appears in the ES and in a similar trend with the first ES peak. All the output intensities of the four peaks increase with the injection current.

The relationships between the injection current and output powers of the four peaks, the peak spacings, and the peak positions are plotted in Figs. 3(a)–3(c), respectively. Peak 1 reaches its threshold at 1.3 mA, rises to a temporary maximum at 2.1 mA, and then drops from 2.1 to 2.4 mA, followed by the lasing of sublevels around peak 2 at 2.5 mA. This indicates that there is a carrier competition relationship between peak 1 and peak 2 and the carrier transfer process between them occurs after 2.1 mA. After an abrupt enhancement from 2.5 to 2.7 mA, the intensity of peak 2 becomes saturated while the rate of increase of the intensity of peak 1 slows down, which is correspondingly ascribed to the subsequent lasing of peak 4. According to the clamping impact on peak 1 and peak 2, at the low excitation density, peak 4 has a direct influence on peak 2, while the slightly impacted peak 1 can be assigned to the carrier competition between peak 2 and itself. Meanwhile, as peak 3 lases at 3.3 mA, peak 4 also experiences a slow elevation due to the carrier coupling between peak 4 and peak 3. When the current increases further to 3.8 mA, the saturated peak 2 has a steady augmentation again and all peaks have a nearly linear enhancement afterward. The phenomenon that

peak 1 and peak 4 increase at the same rate indicates that a strong carrier transition exists at higher injection rate.

In Fig. 3(c), three dashed line are used to indicate the movement trends. With an increase of the injection level, peak 2 splits from peak 1 around 2.3 mA, peak 4 originates from peak 2 at 2.6 mA, and subsequently peak 3 originates from peak 4 at 2.8 mA. As can be clearly seen in the plot, peak 1 has a blueshift in the injection range from 1.2 to 2.3 mA. Peak 2 lases and consumes carriers in sublevels between peak 1 and itself. Due to the Gaussian distribution of IHB, more carriers are available around peak 1 than peak 2, so a rapid blueshift of peak 2 and a slight redshift of peak 1 provide more carriers for their increasing output, leading to the dramatic enlargement of their peak spacing in Fig. 3(b).

At 2.8 mA, the stimulated peak 4 has a clamping impact on peak 2, causing the slowdown of the blueshift rate of peak 2. At 3.3 mA, peak 3 turns on and peak 2 is clamped so strongly that an opposing redshift occurs. The blueshifts of both peak 3 and peak 4 can be attributed to the escalating material gain around the central ES. Meanwhile, due to the gain saturation effect, the peak positions of the four peaks gradually become stable. The oscillation of spacing between peak 1 and peak 2 in Fig. 3(b) is contributed by the carrier relaxation from themselves to fill the breach of carriers needed by peak 4 and peak 3. Simultaneously, the spacing between peak 3 and peak 4 first increases because insufficient carriers between them are available. With more carriers relaxing from the WL into levels around peak 3 and peak 4, carriers in them are abundant for emitting, resulting in not only the stability of the gap between them but also the reduction of their impacts on peak 1 and peak 2. The spacings between peaks are fitted in Fig. 3(d) to investigate the relationship between the four peaks more specifically. Marked clearly, the three peak spacings (peak 2 to peak 1, peak 4 to peak 2, and peak 4 to peak 3) reach zeros at 2.29, 2.61, and 2.81 mA, respectively, agreeing well with the qualitative illustration in Fig. 3(c) as well as all critical points in the analysis of Figs. 3(a)–3(c).

The results in Fig. 3 can be explained also by using the coupled theory [3,4,11] and the spectral dynamics in the time domain of eight selected currents are also investigated in Fig. 4 to give a more convincing illustration. Without loss of generality, QDs with different sizes are divided into three grades, normal-size QDs (NQDs), LQDs, and SQDs. The central energies of the ES and GS are 0.840 and 0.792 eV, respectively; the four sets in Fig. 3(c) have their corresponding QDs sizes, i.e., $E1$ for the GS levels of NQDs, $E2$ for the GS levels of SQDs, $E3$ for the ES levels of LQDs, and $E4$ for the ES levels of NQDs.

As shown in Figs. 3(a) and 3(c), when the excitation is smaller than 1.3 mA, electronic wave function overlap is negligible because the carrier density is in a low level. From 1.3 to 2.29 mA, with more and more carriers accumulating in all subbands, the coupled channels between them are established. With the largest number of empty states and the smallest carrier transferring time, $E1$ accumulates more carriers than other grades and lases first [Figs. 4(a) and 4(b)]. At 2.29 mA, due to the Pauli exclusion effect in $E1$, the carrier transfer process from $E1$ to $E2$ ($E1E2$) is enhanced and overcomes the $E2$ to $E1$ process ($E2E1$), increasing the number of carriers in $E2$, leading to the stimulation of peak
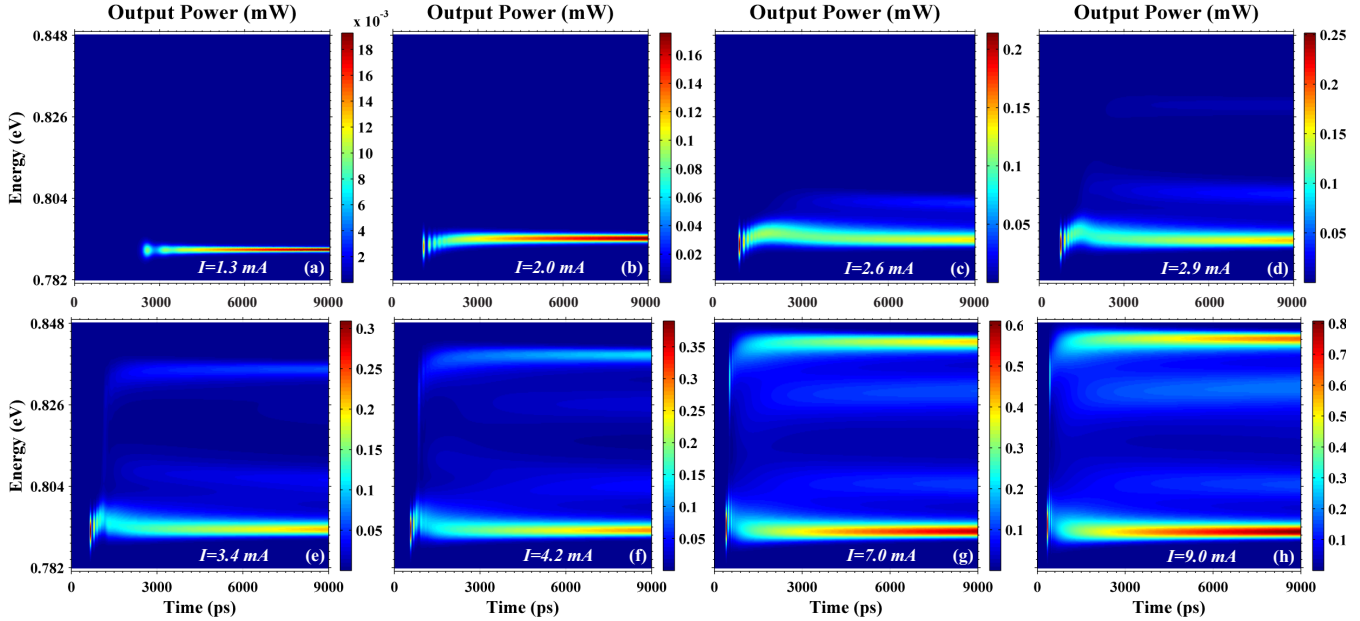
FIG. 4. (Color online) Selected time domain spectrum dynamics with the injection current marked in each figure.

2 in $E2$ at 2.5 mA [Fig. 4(c)]. The $E1E2$ transfer process is a coupling effect between the GS of NQDs and GS of SQDs; it is enhanced first because they have much closer electronic wave functions.

At 2.61 mA, a stronger connection is built between the ES of LQDs and GS of SQDs, similarly causing the emission of peak 4 around $E3$ at 2.8 mA. With reference to Fig. 4(d), peak 4 occurs nearly 900 ps after the lasing of peak 2. As the excitation density increases, under the driving of the Pauli exclusion effect around $E3$, peak 4 moves to partially blocked subgroups at higher energies. Meanwhile, as indicated by the dotted line that connects peak 4 and peak 3, the weak-coupling channels among the high- and low-energy levels in $E3$ are built at 2.81 mA, consequently resulting in the radiation of peak 3 at 3.3 mA in Fig. 3(c), which is additionally supported by the dynamic spectrum after 6500 ps of Fig. 4(e). It is also worth mentioning that the movement of peak 4 from $E3$ to $E4$ is partly contributed by the intradot relaxation from the GS to the ES of NQDs, i.e., $E1$ to $E4$. Taking the linear relationship between peak 4 and peak 1 in Fig. 3(a) as additional evidence, the conclusion can be drawn that the emission of peak 4 is mainly influenced by the intradot relaxing carriers from peak 1 when the injection rate is higher than 3.3 mA.

As peak 4 enters the $E4$ zone, obviously peak 3 has an almost synchronous blueshift with peak 4 [Fig. 3(c)] and the spacing between them becomes gradually stable after 3.8 mA [Fig. 3(b)], indicating that interdot relaxing channels are set up between levels on the ES of NQDs and the ES of LQDs, for which additional evidence can be easily found in Figs. 4(e)–4(h). However, for the injection current located in the range from 3.4 to 3.8 mA, carriers in $E2$ still easily transfer to $E3$, causing the further clamping of peak 2 [Fig. 3(a)]. After the tied interrelation between $E4$ and $E3$ is founded, more occupied levels in $E3$ reduce the possibility for carriers to transfer from $E2$ to $E3$, releasing the clamping of peak 2, which subsequently has a slow increase with the injection rate.

Under dense excitation, there is almost no difference between the spacing between peak 2 and peak 1 and that between peak 4 and peak 3 [Fig. 3(b)] owing to the similar interdot couplings.

B. Comparison between spectra of CQDLs and UQDLs

By setting the Gaussian index matrix $G_{ES_n}G_{GS_k}$ as an identity matrix, the off-diagonal components of the matrix are zeros, meaning that the relaxation times between separated levels of ES_n and GS_k ($k \neq n$) are infinitely long, which results in the complete blocking of channels between them; then the PCMPREM can be used to simulate an UQDL with the same parameters as a CQDL. The thresholds of the given CQDL and UQDL are observed to be 1.3 and 6.8 mA, respectively. For comparison, the spectra of the CQDL and UQDL at 1.3 and 6.8 mA are given in Fig. 5.

At 1.3 mA, the higher output powers at all levels as well as the radiative peak of the CQDL [Fig. 5(a)] suggest a much higher internal carrier efficiency. In Fig. 5(b), which is different from Ref. [11], the coupled spectrum does not show a redshift
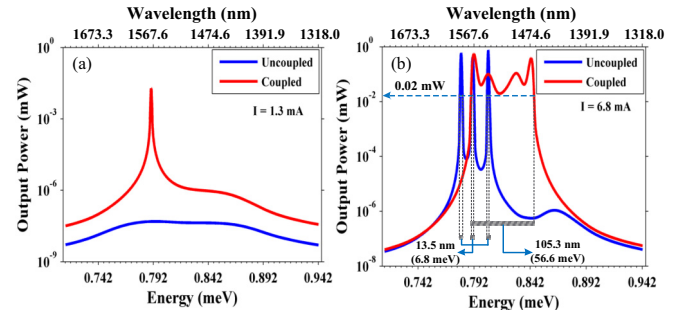

FIG. 5. (Color online) Comparisons between spectra of CQDLs and UQDLs under two injection currents (a) 1.3 mA and (b) 6.8 mA. The corresponding wavelength of the labeled energy levels are marked for a better understanding of the comparison results.

but a significantly improved emission at higher energies. By defining a mode whose power is larger than $0.02\,\mathrm{mW}$ as an available mode, the CQDL has a much flatter output over a broader range of more than $105.3\,\mathrm{nm}$ ($56.6\,\mathrm{meV}$), covering the low loss window for fiber transmission, while the UQDL has only three narrow windows with a total bandwidth of $13.5\,\mathrm{nm}$ ($6.8\,\mathrm{meV}$) around $1550\,\mathrm{nm}$ ($0.801\,\mathrm{eV}$). With the cavity mode spacing being $0.76\,\mathrm{meV}$, nearly 74 longitude modes exists in the CQDL while only 8 or fewer modes can be coupled in the UQDL. Due to their wideband spectra and low threshold, CQDLs can be excellent candidates for wideband light sources with high power efficiency for dense wavelength division multiplexing of optical communication as well as on-chip optical signal processing.

IV. CONCLUSION

In summary, with both IHB and HB effects being considered, a PCMPREM with a Gaussian index matrix was established to simulate the both spectral and carrier transfer characteristics of $1.55-\mu\mathrm{m}$ InAs/InP CQDLs systems. After numerically solving the PCMPREM with the fourth-order Runge-Kutta method, a four-peak output of the CQDL was observed and explanations were given in terms of both carrier competition theory and coupled theory. As the injection

current increases, strong interaction channels are gradually established between the GS of NQDs and the GS of SQDs, the GS of SQDs and the ES of LQDs, higher and lower ESs of LQDs, the GS of NQDs and the ES of NQDs, and the ES of NQDs and the ES of LQDs. It is possible to change the carrier transfer characteristics by varying the injection current and subsequently to optimize the output spectra of the CQDLs through our PCMPREM. This paper gives a systematic understanding of the operation of CQDL systems. Meanwhile, calculated spectra show that CQDLs have significant advantages over UQDLs such as a much lower threshold, higher internal carrier capture efficiency, and flatter output over a much wider band, turning out to be excellent light sources for not only long-haul ultrahigh capacity optical communications, but also on-chip photonics integrated circuits with low power consumption.

[1] N. Kirstaedter, N. N. Ledentsov, M. Grundmann, D. Bimberg, V. M. Ustinov, S. S. Ruvimov, M. V. Maximov, P. S. Kop'ev, Z. I. Alferov, and U. Richter, Electron. Lett. **30**, 1416 (1994).

[2] Z. Mi, P. Bhattacharya, and S. Fathpour, Appl. Phys. Lett. **86**, 153109 (2005).

[3] Y. I. Mazur, J. W. Tomm, V. Petrov, G. G. Tarasov, H. Kissel, C. Walther, Z. Y. Zhuchenko, and W. T. Masselink, Appl. Phys. Lett. **78**, 3214 (2001).

[4] J. W. Tomm, T. Elsaesser, Y. I. Mazur, H. Kissel, G. G. Tarasov, Z. Ya. Zhuchenko, and W. T. Masselink, Phys. Rev. B **67**, 045326 (2003).

[5] B. R. Wang, B. Q. Sun, Y. Ji, X. M. Dou, Z. Y. Xu, Z. M. Wang, and G. J. Salamo, Appl. Phys. Lett. **93**, 011107 (2008).

[6] Y. I. Mazur, V. G. Dorogan, E. Marega, Jr., G. G. Tarasov, D. F. Cesar, V. Lopez-Richard, G. E. Marques, and G. J. Salamo, Appl. Phys. Lett. **94**, 123112 (2009).

[7] J. S. Wang, S. H. Yu, Y. R. Lin, H. H. Lin, C. S. Yang, T. T. Chen, Y. F. Chen, G. W. Shu, J. L. Shen, R. S. Hsiao, J. F. Chen, and J. Y. Chi, Nanotechnology **18**, 015401 (2007).

[8] R. Heitz, I. Mukhametzhanov, P. Chen, and A. Madhukar, Phys. Rev. B **58**, R10151(R) (1998).

[9] G. S. Solomon, J. A. Trezza, A. F. Marshall, and J. S. Harris, Jr., Phys. Rev. Lett. **76**, 952 (1996).

[10] V. López-Richard, S. S. Oliveira, and G.-Q. Hai, Phys. Rev. B **71**, 075329 (2005).

[11] B. Shi and Y. H. Xie, Appl. Phys. Lett. **82**, 4788 (2003).

[12] Y. I. Mazur, Z. M. Wang, H. Kissel, Z. Y. Zhuchenko, M. P. Lisitsa, G. G. Tarasov, and G. J. Salamo, Semicond. Sci. Technol. **22**, 86 (2007).

[13] Y. I. Mazur, G. G. Tarasov, and G. J. Salamo, in *Self-Assembled Quantum Dots* (Springer, Berlin, 2008), p. 67.

[14] Y. I. Mazur, V. G. Dorogan, E. Marega, P. M. Lytvyn, Z. Y. Zhuchenko, G. G. Tarasov, and G. J. Salamo, New J. Phys. **11**, 043022 (2009).

[15] C. Paranthoen, J. Cryst. Growth **251**, 230 (2003).

[16] R. Heitz, A. Kalburge, Q. Xie, M. Grundmann, P. Chen, A. Hoffmann, A. Madhukar, and D. Bimberg, Phys. Rev. B **57**, 9050 (1998).

[17] Y. I. Mazur, X. Wang, Z. M. Wang, G. J. Salamo, M. Xiao, and H. Kissel, Appl. Phys. Lett. **81**, 2469 (2002).

[18] K. Veselinov, F. Grillot, C. Cornet, J. Even, A. Bekiarski, M. Gioannini, and S. Loualiche, IEEE J. Quantum Electron. **43**, 810 (2007).

[19] K. Veselinov, S. Loualiche, F. Grillot, and A. Bekiarski, IEE Proc. Optoelectron. **153**, 308 (2006).

[20] A. Markus, J. X. Chen, O. G. Lafaye, J. G. Provost, C. Paranthoën, and A. Fiore, IEEE J. Sel. Top. Quantum Electron. **9**, 1308 (2003).

[21] H. H. Nilsson, J.-Z. Zhang, and I. Galbraith, Phys. Rev. B **72**, 205331 (2005).

[22] M. Sugawara, K. Mukai, Y. Nakata, H. Ishikawa, and A. Sakamoto, Phys. Rev. B **61**, 7595 (2000).

[23] T. W Berg, S. Bischoff, I. Magnusdottir, and J. Mork, IEEE Photon. Technol. Lett. **13**, 541 (2001).

[24] M. Gioannini, A. Sevega, and I. Montrosset, Opt. Quantum Electron. **38**, 381 (2006).

[25] F. Grillot, K. Veselinov, M. Gioannini, I. Montrosset, J. Even, R. Piron, E. Homeyer, and S. Loualiche, IEEE J. Quantum Electron. **45**, 872 (2009).

[26] B. W. Tilma, M. S. Tahvili, J. Kotani, R. Notzel, M. K. Smit, and Eajm Bente, Opt. Quantum Electron. **41**, 735 (2009).

[27] E. W. Bogaart, R. Nötzel, Q. Gong, J. E. M. Haverkort, and J. H. Wolter, Appl. Phys. Lett. **86**, 173109 (2005).